

1 **Revision 3**

2

3 **IRON OXIDATION STATE IN PHYLLOSILICATE SINGLE CRYSTALS USING**  
4 **FE-K PRE-EDGE AND XANES SPECTROSCOPY:**  
5 **EFFECTS OF THE LINEAR POLARIZATION OF THE SYNCHROTRON X-RAY BEAM**

6

7

8 **MANUEL MUÑOZ<sup>a,b\*</sup>, OLIVIER VIDAL<sup>a</sup>, CLÉMENT MARCAILLOU<sup>a</sup>, SAKURA PASCARELLI<sup>b</sup>,**  
9 **OLIVIER MATHON<sup>b</sup>, FRANÇOIS FARGES<sup>c</sup>**

10

11

12

13 <sup>a</sup>*INSTITUT DES SCIENCES DE LA TERRE, CNRS, UNIVERSITE DE GRENOBLE 1, FRANCE*

14 <sup>b</sup>*EUROPEAN SYNCHROTRON RADIATION FACILITY, GRENOBLE, FRANCE*

15 <sup>c</sup>*LABORATOIRE DE MINERALOGIE, CNRS, MUSEUM NATIONAL D'HISTOIRE NATURELLE, PARIS, FRANCE*

16

17

18

19 **Keywords: iron, redox, polarization, XANES, phyllosilicates.**

20 \*Corresponding author. Email: [manuel.munoz@ujf-grenoble.fr](mailto:manuel.munoz@ujf-grenoble.fr)

21

22

23 **Abstract**

24 We investigated the influence of linear polarization of the synchrotron X-ray beam on the  
25 determination of iron oxidation state in phyllosilicates. Fe K-edge XANES spectra and pre-edge  
26 peaks have been recorded for various orientations of single crystals of biotite (Bt), clinocllore  
27 (chlorite group; Cli), talc (Tc) and antigorite (serpentine group; Ant). *Ab initio* XANES  
28 calculations, performed for 6 orientations of the biotite structure, support the experimental results.  
29 Depending on crystal orientation, the experimental results show, 1) important changes both for  
30 XANES and pre-edge peaks, 2) characteristic changes of spectral signatures regardless of the  
31 mineral species, 3) uncorrelated changes between XANES and pre-edge peaks, 4) important  
32 changes of the energy position of pre-edge peaks, but with no significant change for their integrated  
33 areas. Regarding the crystal orientation, the pre-edge peak centroid varies in energy by  $\sim 0.4$  eV in  
34 the case of Bt and Tc, and by  $\sim 0.2$  eV for Cli and Ant. Such variations correspond to  $\#Fe^{3+}$  (i.e.,  
35  $Fe^{3+}/Fe_{total}$ ) of 0.22 and 0.15, respectively. Comparison with the analysis of powdered samples show  
36 that Fe-redox can be generally framed as follows:  $-(2/3)\#Fe^{3+} < \#Fe^{3+}_{(powder)} < +(1/3)\#Fe^{3+}$ . In good  
37 agreement with the so-called “magic angle” theorem for powdered samples, we propose an ideal  
38 orientation of the single crystals that provide similar pre-edge peaks as for powdered samples. With  
39 the wavevector (i.e., beam direction) perpendicular to (100) or (010), measurements should be done  
40 with an angle of  $35^\circ$  between the electric-field vector and the [001] crystal direction. Moreover,  
41 measurements performed with the wavevector perpendicular to (001) systematically result in an  
42 overestimation of  $\#Fe^{3+}$  up to 0.07. Finally, we show that the appropriate positioning of single  
43 crystals reduces the  $\#Fe^{3+}$  uncertainty to the intrinsic error of pre-peak measurements. This  
44 approach opens possibilities for *in situ* analyses of Fe-bearing phyllosilicates in thin sections that  
45 are potentially relevant for scientific fields such as hydrothermal/metallogenic, metamorphic,  
46 meteoritic or environmental mineralogy.

## 47 **1. Introduction**

48 Iron is the most abundant transition metal on Earth, and presents various oxidation states  
49 according to the redox conditions of geological settings: elemental, ferrous and ferric iron, even  
50 Fe(IV) as in amethyst (Di Benedetto et al., 2010). The oxidation state of iron in minerals is a  
51 valuable indicator for the understanding of numerous mineralogical and petrological processes, such  
52 as: *i*) metamorphic conditions prevailing in the continental crust (e.g., Diener and Powell, 2010;  
53 Dyar et al., 2002b; Schmid et al., 2003; Vidal et al., 2006; Vidal et al., 2005); *ii*) ultra-high P-T  
54 conditions prevailing in the Earth's mantle or at the core-mantle boundary (e.g., Andrault et al.,  
55 2010; Canil et al., 1994; Frost and Langenhorst, 2002; McCammon et al., 2004); *iii*) high  
56 temperature conditions of magmatic processes (e.g., Berry et al., 2008; Kelley and Cottrell, 2009);  
57 *iv*) medium temperature and low pressure conditions typical of mid-oceanic ridges (e.g., Andréani  
58 et al., 2008; Marcaillou et al., 2011), or environmental and biomineralogical processes (e.g.,  
59 Benzerara et al., 2005; Brown et al., 2008; Miot et al., 2009).

60 Among the several analytical techniques that can be used to determine the oxidation state of  
61 iron in minerals, XANES spectroscopy presents a large flexibility with beam size (from millimetric  
62 down to a dozen nanometers by STXM; Scanning Transmission X-ray Microscopy), or detection  
63 limits (down to a few tens of ppm), depending on the beam line and/or synchrotron source used.  
64 The pre-edge peaks of XANES have been shown to be extremely sensitive to the oxidation state of  
65 iron (e.g., Bajt et al., 1994; Berry et al., 2003; Farges, 2001; Galois et al., 2001; Petit et al., 2001;  
66 Shulman et al., 1976; Wilke et al., 2001; Wilke et al., 2005). XANES spectroscopy requires the use  
67 of a monochromatic synchrotron X-ray beam, which is generated with a horizontal linear  
68 polarization due to the synchrotron ring geometry. This property of the X-ray beam does not affect  
69 the characterization of mono-, or poly-mineral powders that show randomness in the crystalline  
70 orientation of grains. In contrast, the X-ray absorption spectrum of a single crystal depends on its  
71 orientation relative to the polarized X-ray beam (e.g., Dyar et al., 2001; Dyar et al., 2002a;

72 Henderson et al., 1995; Manceau et al., 1988; Marcelli et al., 2006; Mottana et al., 2002; Schofield  
73 et al., 1998; Van Der Laan et al., 1996).

74 Polarization effects at the iron *K*-edge (pre-edge peak and XANES) for various selected  
75 micas were reported by Dyar et al. (2001) and Mottana et al. (2002). These studies aimed at  
76 reporting uncertainties on the determination of the  $\text{Fe}^{3+}/\text{Fe}_{\text{total}}$  ratio ( $\#\text{Fe}^{3+}$ ) for phyllosilicate single  
77 crystals. Both studies report  $\pm 10\%$  of absolute uncertainty for  $\#\text{Fe}^{3+}$  if the measurement is made for  
78 a crystal with unknown orientation. This uncertainty is much higher than that achievable on  
79 randomly-oriented powders (about  $\pm 3\%$  for octahedral cation exchanges; Wilke et al., 2001). This  
80 is due to the complex dependence of the pre-edge (PE) peak as a function of mineral and beam  
81 polarization. Hence, no satisfactory methodology has been proposed to achieve reliable values for  
82 variably oriented mineral grains in natural rocks.

83 The present study aims at characterizing and quantifying the effect of linear polarization of  
84 the X-ray beam on XANES spectra and PE peaks recorded for phyllosilicate single crystals at the  
85 Fe *K*-edge. Notably, we intend to 1) better explore the angular-dependency without changing the  
86 geometry of detection to avoid possible self-absorption effects, 2) improve data quality with better  
87 signal-to-noise ratio, 3) improve data analysis and  $\#\text{Fe}^{3+}$  determination using calibration curves of  
88 Wilke et al. (2001). The angular dependency is evaluated for six orientations of euhedral biotite  
89 single-crystal, cross-checked with theoretical *ab initio* XANES calculations for a similar structure  
90 (FEFF8.2 package). Then, four single-crystals of biotite, clinocllore, talc and antigorite are  
91 characterized by XANES spectroscopy (Fe *K*-edge) for specific orientations. PE peaks are used to  
92 estimate the variations of the observed  $\#\text{Fe}^{3+}$  according to the crystal orientation. Finally, specific  
93 orientations of single crystals are proposed to measure “powder-equivalent”  $\#\text{Fe}^{3+}$ , and compared to  
94 the so-called “magic-angle” (Pettifer et al., 1990).

## 95 **2. Experimental methods**

### 96 **2.1. Sample descriptions**

97 Four single crystals of biotite (Bt), clinochlore (chlorite group; Cli), talc (Tc) and antigorite  
98 (serpentine group; Ant) were selected from the mineralogy museum of the Institut Dolomieu at the  
99 Université Grenoble 1, France; <http://collections.obs.ujf-grenoble.fr>. They show millimetric to  
100 centimetric euhedral faces, and they are at least 1 mm thick, which enables X-ray absorption  
101 measurements with a probe-size of a few hundreds of micrometers. Each single crystal was cut  
102 perpendicularly to the (001) plane with a micrometric diamond-saw, to permit X-ray measurements  
103 through this oriented section. (001) cleavage is clearly identified for each crystal. The biotite crystal  
104 is translucent to opaque, depending on the thickness of the layers, and shows a typical dark-brown  
105 color. The crystal presents a platy texture with “flexible” plates; its geological origin is  
106 undocumented. The single crystal of talc is translucent, with a pale green color. This crystal was  
107 collected at the Trimouns mines (Luzenac, France). The clinochlore crystal has a dark-green color  
108 with a vitreous luster, and shows relatively massive layers. This crystal was collected in the Zermatt  
109 area in Switzerland. The antigorite is translucent, massive and has a typical green color with a  
110 greasy luster. This crystal was collected in the Mont-Cenis massif in the French Alps.

## 111 **2.2. Chemical analyses**

112 The composition of the crystals has been measured by X-Ray Fluorescence (XRF) analysis  
113 performed with an EDAX Eagle-III micro-XRF at the Institut des Sciences de la Terre (Grenoble,  
114 France). The fluorescence spectra (Fig. 1) were measured for 300 s with a vacuum of 0.3 mbar  
115 using a Rh anode, at 20 kV/400  $\mu$ A. The quantification of the XRF spectra was achieved with the  
116 Vision32 software assuming a calibration based on a set of 12 oxide-, and silicate-standards  
117 certified by Astimex Scientific Limited (MINM25-53 Mineral Mount) to reach less than 3% of  
118 relative uncertainty for the concentration calculations. Element concentrations were obtained after 6  
119 or 7 iterations between the matrix adjustment (i.e., concentration of major elements) and the  
120 theoretical calculation of the corresponding XRF spectrum. The iterative calculation was stopped  
121 when the predicted and measured intensities of the fluorescence lines differed by less than 0.1%.

122 The chemical analyses of the four starting crystals, expressed in weight percent (wt.%) and in atom  
123 per formula unit (a.p.f.u.), are listed in Table 1. Following the XANES and PE peak data reduction  
124 detailed later in this article, the iron contents were calculated assuming that iron in Bt, Cli and Tc is  
125 in the ferrous state (FeO basis), and iron in Ant is in the ferric state (Fe<sub>2</sub>O<sub>3</sub> basis). Iron oxide  
126 contents of Bt, Cli, Tc and Ant are 3.88, 2.86, 1.28 and 1.16 wt.%, respectively.

### 127 **2.3. X-ray absorption spectroscopy**

128 Iron speciation (*K*-edge) was measured by X-ray absorption spectroscopy at the BM29  
129 beamline – now moved on BM23 – of the ESRF (European Synchrotron Radiation Facility;  
130 Grenoble, France). The storage ring was operating in the 16-bunch mode with an average current of  
131 75 mA. X-rays were generated using a bending magnet, and monochromatized with a double-  
132 crystal, fixed exit Si(111) monochromator. The low vertical divergence of the X-rays leads to a  
133  $\Delta E/E$  of  $2.8 \times 10^{-4}$ , providing an energy resolution of  $\sim 1.99$  eV at 7112 eV. XANES spectra were  
134 collected at the iron *K*-edge in the fluorescence mode with a 13-element Ge-detector located on the  
135 horizontal plane at 90 degrees from the incident X-ray beam direction. The sample surfaces were  
136 positioned perpendicular to the X-ray beam to minimize self-absorption (Pfalzer et al., 1999).  
137 Crystals were rotated around the propagation axis of the X-ray beam so that the geometry of  
138 detection remains identical for all measurements (i.e., whatever the angle of rotation, the angle  
139 between the sample surface and the incident beam is 90°). The energy sampling step for the  
140 acquisition of the XANES spectra was optimized to properly resolve the different features. A first  
141 linear region with a 5 eV step was used from 7070 eV to 7100 eV to collect a large pre-edge region  
142 required for robust data normalization. Then we defined a second region that evolves polynomially  
143 from 0.5 to 1 eV, respectively from 7100 to 7250 eV, to properly sample the PE peak and “white-  
144 line” regions. XANES normalization and fits of PE features were performed in batch processing  
145 mode thanks to the XasMap package, originally dedicated to dispersive micro-XANES mapping  
146 applications (Muñoz et al., 2006; Muñoz et al., 2008; Pascarelli et al., 2006). According to the work

147 of Wilke et al. (2001), the Fe-K PE peaks were fitted between 7108 and 7118 eV using Gaussian-  
148 Lorentzian (GL) amplitude sum functions (i.e., pseudo-Voigt functions), which consider both the  
149 Lorentzian broadening imposed by the core-hole lifetime and the Gaussian experimental resolution.  
150 Considering the energy resolution of our experimental data, two peaks were sufficient to properly  
151 fit the electronic transitions in the pre-edge features, i.e., local electric quadrupole transitions  $1s \rightarrow$   
152  $3d$ , and/or local and non-local electric dipole transition  $1s \rightarrow p-d$  hybridized orbitals (see Cabaret et  
153 al., 2010 and references therein). For each individual GL peak, we fixed the G/L ratio and the full-  
154 width half-maximum (FWHM) to their best mean values obtained for the whole data set: 50% and 2  
155 eV, respectively. It should be noted that energy positions and intensities modeled from PE features  
156 have little physical significance since they result from the convolution of two distinct functions  
157 (Gaussian and Lorentzian) that refer to different physical properties. Farges et al. (2004) showed  
158 that the type of baseline used for the analysis of a pre-edge peak mainly affects its intensity but not  
159 significantly the energy position of its centroid. Here, the baseline was empirically adjusted by the  
160 tail of a Gaussian function since, for the energy range used for pre-edge fitting, the Lorentzian  
161 percentage of the pseudo-Voigt naturally tends to 0 when the G/L ratio is not fixed. This method  
162 provides best results in the peak-fitting procedure and is the least sensitive to the intrinsic noise of  
163 the data. Finally, according to Wilke et al. (2001), the pre-edge variogram and calibration was based  
164 on four powdered model compounds presenting different types of iron speciation, namely staurolite  
165 ( $^{[4]}\text{Fe}^{2+}$ ), unoxidized olivine ( $^{[6]}\text{Fe}^{2+}$ ), andradite ( $^{[6]}\text{Fe}^{3+}$ ) and sanidine ( $^{[4]}\text{Fe}^{3+}$ ). This approach can be  
166 used because no other local geometry (like square planar, cubic or antiprism geometry, etc.) is  
167 expected around Fe in our phyllosilicates.

### 168 **3. Results**

#### 169 **3.1. Detailed polarization dependence for biotite**

##### 170 **3.1.1. *Ab initio* XANES calculations**

171 *Ab initio* XANES calculations were performed to evaluate the variations of XANES spectral  
172 features as a function of the orientation of a single crystal relative to the horizontally polarized X-  
173 ray beam. Calculations were achieved with the FEFF8.2 software (Ankudinov et al., 1998; Rehr et  
174 al., 1992) at the Fe *K*-edge for biotite, based on the structure refinement of Sassi et al. (2008). A  
175 self-consistent field (SCF card) multiple-scattering procedure was used to model charge transfer  
176 between atoms during the photo-electric process up to 3.3 Å. Full multiple scattering (FMS card)  
177 calculations were performed for the first eight shells of atoms (up to 4.6 Å) to achieve a close match  
178 between the calculated and experimental spectrum of the powdered biotite. POLARIZATION and  
179 ELLIPTICITY cards were used to simulate different orientations of the crystal exposed to a  
180 horizontally-polarized X-ray beam.

181 Crystal positioning can be described by two vectors that characterize the polarized X-ray  
182 beam: the wavevector  **$\mathbf{k}$**  that indicates the direction of the  
183 horizontal beam, and the electric-field vector  **$\mathbf{E}$**  that is also horizontal, but perpendicular to the  
184 wavevector (see Figure 2). With  **$\mathbf{k}$**  parallel to the ***a***-axis of the structure,  **$\mathbf{E}$**  can be either parallel to the  
185 ***c***-, or ***b***-axis (see Figure 2a and 2b, respectively). The same reasoning can be conducted if  **$\mathbf{k}$**   
186 is parallel to the ***b***-axis (i.e., parallel to ***a***-, or ***c***-axis), and to the ***c***-axis (i.e., parallel to ***a***-, or ***b***-axis).  
187 Then, six XANES spectra were computed for the six orientations (Fig. 3a). To distinguish between  
188 them, each spectrum is labeled with two letters. The first letter indicates the crystallographic axis  
189 that is parallel to the wavevector, and the second refers to the crystallographic axis parallel to the  
190 electric-field vector.

192 The FEFF8.2 simulations mainly show two different shapes of XANES spectra among the  
193 six orientations (Fig. 3a). These results show that XANES anisotropy is only a function of the  
194 orientation of  **$\mathbf{k}$**  relative to the structure, regardless of the direction of the X-ray beam. This  
195 observation is consistent with the *K*-edge probed here, i.e., the excitation of 1s electrons (spherical

196 orbital) that leads to a dependence only as a function of  $\theta$  and the crystal structure in its  
197 corresponding direction. Thus, we observe a perfect equivalence for the spectra *ac* and *bc*, *ab* and  
198 *cb*, and *ca* and *ba*, respectively. Moreover, the pairs of spectra *ab-cb* and *ca-ba* are also very similar  
199 to each other. In comparison, the pair *ac-bc* shows major differences, with a strong decrease and  
200 widening of the D feature, a slight widening of E, and a significant shift towards lower energies for  
201 the F feature. Note that, although the nature of electronic transitions is different, these observations  
202 could be compared to polarized optical microscopy observations, for example for the pleochroic  
203 properties of biotite. Indeed, light absorption is strong when the wavevector is perpendicular to  
204 (001), *ca* or *cb* orientations, as well as for *ab* or *ba* orientations (dark brown color). In contrast, light  
205 is less absorbed for *ac* or *bc* orientations (clear brown color). Such similarities most likely refer to  
206 the atomic density that is observed from a 6-fold coordinated iron in the biotite structure: atomic  
207 density in the direction [001] is much lower compared to [100] or [010]. Another comparison can  
208 be made with isotropic minerals (cubic lattice): optical pleochroism is not observed, while polarized  
209 XANES spectroscopy shows similar spectral signatures regardless of crystal orientation (e.g.,  
210 Bordage et al., 2010).

### 211 3.1.2. Experimental measurements (XANES and pre-edge peaks)

212 Observations made for the calculated XANES spectra were crosschecked with experimental  
213 measurements. For the six orientations defined above, experimental XANES spectra for biotite were  
214 collected at the Fe-*K* edge. The euhedral faces of the single crystal were used as benchmarks for its  
215 exposure to the X-ray beam. As predicted by theory, Figure 3b shows two well-contrasted XANES  
216 shapes over the six orientations. For each group, the XANES overlap each other nearly perfectly: on  
217 one hand, the spectra labeled *ac* and *bc* (in grey), on the other hand the spectra labeled *ab*, *cb*, *ca*  
218 and *ba* (in black). Between these two contrasted shapes, changes observed for the features B, C, D,  
219 E and F are very close to those obtained from *ab initio* calculations.

220 Pre-edge features are displayed in the zoom inserted in Figure 3b. This figure shows that PE  
221 peaks obtained for the orientations *ab* and *ba* (i.e., horizontal silicate sheets; see the lines with black  
222 and white squares) have their centroid located at lower energies compared to the others. The  
223 difference observed between *ca-cb* and *ac-bc* is simply due to their different baselines because of  
224 the different spectral signatures in the white-line regions. However, similar values are observed for  
225 their PE peak centroids (see Table 2).

226 As a consequence, while XANES spectra show different spectral signatures for the *ac-bc*  
227 pair, the PE peaks show distinct shapes for the *ab-ba* pair. These contrasted observations between  
228 the XANES and PE peaks are most likely due to their different photoelectron probing mechanism:  
229 1) medium range order (i.e.,  $\sim 3-10 \text{ \AA}$ ) around the photo-absorber for the XANES; 2) the local  
230 geometry of the 3d molecular orbitals (i.e.,  $< 3 \text{ \AA}$ ) for the PE peaks (considering only the crystal  
231 field split transitions). The behavior of PE peaks can no longer be compared to optical microscopy  
232 as for the XANES part of the spectrum (above the absorption edge). In the case of a given cubic  
233 iron-bearing structure (such as garnet or wustite, etc.), the pre-edge varies while the XANES region  
234 remains unchanged (Bolfan-Casanova et al., 2012; Bordage et al., 2010; Heumann et al., 1997).

### 235 **3.2. Comparative analysis for biotite, clinocllore, talc and antigorite**

#### 236 **3.2.1. XANES polarization dependence**

237 According to the detailed study of polarization dependence for biotite (*ab initio* calculations  
238 and experimental measurements), four series of spectra have been collected, with variable  
239 orientations, for the biotite, clinocllore, talc and antigorite single crystals (Figure 4a, 4b, 4c and 4d,  
240 respectively). Each crystal was first oriented with a vertical slice perpendicular to the beam (see  
241 Figure 2a); this orientation is labelled *ac-bc* because of the spectral equivalence observed (Fig 3b).  
242 Such orientation is noted as  $0^\circ$  in Figure 4. Then, the crystals were progressively rotated in steps of  
243  $15^\circ$  to reach a  $90^\circ$  position where the horizontal slice is perpendicular to the beam (i.e., *ab-ba*).  
244 Another spectrum was collected with (001) perpendicular to the beam (i.e., *ca-cb*). Finally, two

245 more spectra are shown, which correspond to, 1) the powdered mineral, and 2) the average of the  
246 three “end-member” spectra. These two spectra are systematically identical for each mineral, which  
247 means that the spectrum of a randomly oriented powder is equivalent to the average of the three  
248 end-members.

249       Figures 4a, 4b and 4c show that the XANES spectra for Bt, Cli and Tc are quite similar for a  
250 given orientation. For these three minerals, the angular dependence of the different features is  
251 similar to the description predicted by FEFF (Figure 3a). The feature A indicates the location of PE  
252 peaks (detailed in Figure 5). Features B, C and D have relatively similar intensities at 0°, while D  
253 becomes significantly higher for *ab-ba* (90°) and *ca-cb*. Moreover, from the 0 to 90°, feature E  
254 slightly shifts towards lower energies and becomes narrower, while feature F shifts towards higher  
255 energies. The strong similarities between the XANES spectral signatures of Bt, Cli and Tc are  
256 consistent with the similar atomic local structure around Fe in these minerals, where iron is mainly  
257 located in the octahedral sites, in the tri-octahedral layer of T-O-T sheets. On the other hand,  
258 XANES spectra of the antigorite only show small variations depending on the crystal orientation  
259 (see Fig. 4d). Compared to Bt, Cli and Tc, the XANES spectra of antigorite are clearly different,  
260 most likely because of a well contrasted local structure of iron in this mineral – particularly in the  
261 direction parallel to *c* – in which it is located in octahedral sites, in the tri-octahedral layer of T-O  
262 sheets. Even so, such comparison of tri-octahedral T-O vs. T-O-T structures should highlight some  
263 structural, and spectral, similarities in directions parallel to (001) for which the atomic landscape of  
264 iron are similar. Therefore, another explanation could be the presence, in weak proportion, of 4-fold  
265 coordinated iron in this mineral. This hypothesis is reinforced by the occurrence of high amounts of  
266 Fe<sup>3+</sup> relative to the Fe<sub>total</sub> (see further in Figure 6), and agrees with the evidence of weak proportions  
267 of tetrahedral iron proposed by Marcaillou et al. (2011) in experimental serpentines.

### 268 **3.2.2. Pre-edge polarization dependence**

269 Figures 5a, 5b, 5c and 5d show the baseline-subtracted PE peaks that correspond to the  
270 XANES spectra in Figure 4: Bt, Cli, Tc and Ant, respectively. Open circles indicate the series from  
271 0 to 90° as well as the *ca-cb* orientation, black diamonds and black circles indicate the average and  
272 powder spectra, respectively. Each PE peak is fitted using two pseudo-Voigt functions (dotted  
273 lines), labeled A' and A'' for the low and high-energy peak, respectively, and the fit results are  
274 represented by solid lines. For each PE peak, the centroid energy position, integrated area and  
275 corresponding #Fe<sup>3+</sup> are listed in Table 3.

276 As observed for the XANES spectra, the evolutions of the PE peak features as a function of  
277 crystallographic orientation are quite similar for the Bt, Cli and Tc. Rotating the samples from 0 to  
278 90° by steps of 15° leads to a progressive decrease in intensity of the peak A'' relative to A'.  
279 However, in contrast to the XANES, similarities are observed between *ac-bc* and *ca-cb*, while *ab-*  
280 *ba* is clearly different. For *ac-bc* and *ca-cb*, feature A' is slightly higher than A''. For *ab-ba*, feature  
281 A' is much more intense than the feature A'', so the centroid energy is significantly shifted towards  
282 lower energies. In the case of antigorite, the intensity of the peak A' is negligible while the intensity  
283 of the peak A'' is much higher, corresponding to a higher energy position of the PE peak centroid;  
284 as for the XANES, only slight variations are observed with the crystal orientation.

285 In Figure 6, integrated area *versus* centroid energy are displayed in a variogram similar to  
286 the one presented by Wilke et al. (2001). This variogram shows the end-member positions that  
287 correspond to the four model compounds used in this study, and thus to the different Fe-speciation  
288 end-members: <sup>[4]</sup>Fe<sup>2+</sup>, <sup>[6]</sup>Fe<sup>2+</sup>, <sup>[6]</sup>Fe<sup>3+</sup>, <sup>[4]</sup>Fe<sup>3+</sup>. Each model compound is located in a grey circular  
289 region that is larger than the precision of the method (i.e., ± 0.05 eV in energy). This variogram also  
290 shows the values obtained for the different orientations of the Bt, Cli, Tc and Ant crystals, from 0 to  
291 90°. The values obtained are located near the line labeled [VI], which corresponds to mixtures  
292 between <sup>[6]</sup>Fe<sup>2+</sup> and <sup>[6]</sup>Fe<sup>3+</sup>. This observation confirms that iron is exclusively six-fold coordinated  
293 in these minerals. Depending on their orientation, Bt, Cli and Tc show centroid positions varying

294 from the  $^{[6]}\text{Fe}^{2+}$  end-member to around 0.4 to 0.6 eV towards higher energies. The differences in  
295 energy-range observed for these minerals are likely due to slight variations of either, i) the local  
296 structure around  $\text{Fe}^{2+}$  in octahedral sites, e.g., site distortions, or ii) the averaged oxidation state of  
297 iron. In contrast, centroid values obtained for antigorite are located around 7114.4 eV, close to the  
298  $^{[6]}\text{Fe}^{3+}$  end-member and slightly above the [VI]-axis, which suggests that iron is mostly ferric and  
299 octahedrally coordinated in this crystal. The relatively high integrated area values observed for  
300 antigorite might be due to a weak proportion of tetrahedral iron, or possibly distortions of the  
301 octahedral sites due to the large amount of ferric iron in the structure, which may lead to less  
302 centrosymmetric site geometry.

303         The conversion from the centroid energy and integrated area, respectively to iron oxidation  
304 state and coordination number is not straightforward. In particular, centrosymmetry is not a direct  
305 function of the coordination. However, the phyllosilicates studied only present tetrahedral or  
306 octahedral coordination geometries. This allows us to interpret the centrosymmetry information in  
307 terms of averaged coordination numbers. Wilke et al. (2001) show that the relation between PE  
308 peak intensity and averaged coordination number is quasi-linear, whereas the calibration curve for  
309 the oxidation state quantification is not (see their figures 6 and 7). In the present study, we use their  
310  $^{[6]}\text{Fe}^{2+}$ – $^{[6]}\text{Fe}^{3+}$  calibration curve to derive  $\#\text{Fe}^{3+}$  values. Our results reveal that crystal orientation  
311 does not strongly affect the PE peak intensities, so that we mainly focus on the iron oxidation state  
312 determination based on PE peak energies.

### 313 **3.2.3. $\#\text{Fe}^{3+}$ polarization dependence**

314         Figure 7a shows the dependence of the centroid energy according to the rotation angle  
315 around the X-ray propagation direction. For each sample, including antigorite, the centroid position  
316 decreases in energy from  $0^\circ$  to  $90^\circ$ , in perfect agreement with the qualitative observations made on  
317 the PE peak shapes in Figure 5. Benchmarks for the  $^{[6]}\text{Fe}^{2+}$ , and  $^{[6]}\text{Fe}^{3+}$  end-members are represented  
318 as grey strips, with a width equivalent to the diameter of the grey circles in Figure 6. Since the

319 intensity of the electric-field vector oscillates in a plane defined by itself and the wavevector (see  
320 Figure 2), the periodicity for the crystal rotation relative to the X-ray beam is  $180^\circ$  (i.e., the  
321 maximum contrast between  $0$  and  $180^\circ$  is observed at  $90^\circ$ ). Therefore, each spectral signature  
322 (XANES and/or PE peak) shows an angular dependence with a periodicity of  $180^\circ$ , and each series  
323 of centroid energies ( $y$ ) as a function of the angle ( $x$ ) was fitted with a sine function defined as  
324 follow:

325 Eq. 1

326 where  $\alpha$  is the median value of the centroid energy range, and  $\beta$  is the amplitude of the variations.  
327 The angular frequency ( $\omega$ ) and the phase-shift ( $\varphi$ ) are, respectively, equal to  $2\pi/180$  and  $\pi/2$ . The  
328 parameters  $\alpha$  and  $\beta$  for the data series of Bt, Cli, Tc and Ant are both listed in Table 4. For each  
329 crystal, the range of values obtained for the centroid energies is defined by  $\alpha \pm \beta$ , and the energy  
330 range is equal to  $2\beta$  (see Table 4). Consequently, the maximum variation of the centroid energies is  
331 observed for talc (0.40 eV) and biotite (0.39 eV). The lowest variation is observed for antigorite  
332 (0.16 eV), and an intermediate value is observed for clinocllore (0.25 eV). For comparison, the  
333 values of the centroid energy obtained for the powdered minerals are reported as horizontal grey  
334 strips labelled “powder” in Figure 7a. In the  $0$ - $90^\circ$  range, the strips intersect the sine models (Eq. 1)  
335 at around  $35 \pm 5^\circ$  (considering about 0.05 eV of uncertainty). Based on that result, and on  
336 similarities observed between PE peaks  $ac-bc$  and  $ca-cb$  (Figure 5), the centroid energy equivalent  
337 to that of a powdered sample can be empirically approximated as:

338 Eq. 2

339 where  $(\alpha + \beta)$  is the centroid energy for the orientations  $ac-bc$  and  $ca-cb$ , and  $(\alpha - \beta)$  is the centroid  
340 energy for the orientation  $ab-ba$ . Values obtained for the “powder-equivalent” centroid energies are  
341 listed in Table 4.

342 Centroid energy values obtained for the oriented crystals were converted into  $\#Fe^{3+}$  based on  
343 the  $^{[6]}Fe^{2+} - ^{[6]}Fe^{3+}$  calibration curve of Wilke et al. (2001). Note that these  $\#Fe^{3+}$  values are not

344 “real” but “apparent” values, since all the Fe cations are simultaneously probed during  
345 measurements, whatever the crystal orientation. Therefore, these apparent values do not correspond  
346 to a sort of selective view of the different cations in the structure (sensitive to site-ordering for  
347 example), but they are related to the crystal-field in the  $O_h$  geometry relative to the electric-field of  
348 the X-ray beam. For each orientation of the crystals, the apparent  $\#Fe^{3+}$  has been reported in Table 3  
349 as well as in Figure 7b. As for the centroid energies, the apparent  $\#Fe^{3+}$  values ( $y$ ) were fitted as a  
350 function of the angle ( $x$ ) using the same type of equation:

351 
$$\text{Eq. 3}$$

352 in which  $\gamma$  is the medium value of the  $\#Fe^{3+}$  variability,  $\delta$  is the amplitude of the variations. The  
353 angular frequency  $\omega$  and the phase-shift  $\varphi$  are equivalent to the ones used in Eq. 1. The parameters  $\gamma$   
354 and  $\delta$  for the data series of Bt, Cli, Tc and Ant are both listed in Table 4, as well as  $2\delta$  that  
355 represents the variability range for  $\#Fe^{3+}$  (i.e.,  $\Delta\#Fe^{3+}$ ). This variability range is 0.22 for Bt and Tc  
356 and 0.14 and 0.15 for Cli and Ant, respectively. At  $35^\circ$ , the  $\#Fe^{3+}_{eq}$  values are 0.15, 0.17 and 0.18  
357 for Bt, Cli and Tc, respectively. These results indicate that iron is mainly in the ferrous state in these  
358 minerals. In contrast, iron in the antigorite characterized in this study is much more oxidized, with a  
359  $\#Fe^{3+}_{eq}$  of 0.81. The values of  $\#Fe^{3+}_{eq}$  obtained at  $35^\circ$  (Table 4) are in excellent agreement with  
360 those obtained for the powdered minerals (Table 3).

361

#### 362 **4. Discussion**

363 In agreement with the results of Dyar et al. (2001), the experimental and theoretical data  
364 obtained for the phyllosilicates investigated here highlight important changes in the spectral  
365 signatures with the orientation of the single crystals. Furthermore, we show additional information  
366 such as the independent behavior between the XANES and PE peak shapes. For each crystal  
367 investigated, the orientation  $ac-bc$  (i.e., electric-field vector parallel to the  $c$ -axis) shows contrasted  
368 XANES compared to the other crystallographic orientations, while the orientations  $ab-ba$  and  $ca-cb$

369 are quite equivalent to each other. Concerning the PE peaks, we show that the positioning *ab-ba* is  
370 different from the others, whereas *ca-cb* and *ac-bc* are equivalent to each other. These uncorrelated  
371 variations between the XANES (features above the edge) and the PE peak regions are due to  
372 different types of interactions between the excited electron and the electronic/atomic structure  
373 around the photoabsorber. On one hand, the XANES region reflects photoelectric multiple-  
374 scattering effects at medium-range distance around the photoabsorber (Ankudinov et al., 1998; Rehr  
375 et al., 1992; Rehr et al., 1995). So, the differences or similarities observed in the XANES shapes are  
376 most likely due to the atomic “landscape” in the direction of  $\mathbf{a}$ . For *ab-ba* and *ca-cb*,  $\mathbf{a}$  is either  
377 parallel to  $\mathbf{a}$  or  $\mathbf{b}$ . The photoelectric wave associated to the excited photon mostly interacts with  
378 atoms in the octahedral plane of the TOT layer, i.e., within the (001) plane, and therefore “sees”  
379 relatively similar atomic landscape. In contrast, for *ac-bc*, the photoelectric wave most likely  
380 propagates perpendicularly to the TOT layers, i.e., in the [001] direction, and therefore sees well  
381 contrasted atomic density/landscape when compared to the other orientations. On the other hand,  
382 the PE peaks are related to 1s-3d (quadrupolar) and/or 1s-4p (dipolar) electronic transition (Dräger  
383 et al., 1988; Heumann et al., 1997; Shulman et al., 1976; Westre et al., 1997), and thus can be  
384 considered as a short-range structural probe around the photoabsorber (electronic cloud; below 3  
385 Å). Differences observed between the pre-edge peaks likely result from the geometry of the  
386 hybridized orbitals in crystal-field splitting of the octahedral sites (e.g., Cabaret et al., 2010; Galois  
387 et al., 2001). A decrease of the average symmetry degree of iron sites, such as distortions or the  
388 occurrence of tetrahedral iron, may cause strong changes in the pre-edge shapes depending on the  
389 crystal orientation.

390 The XANES spectrum of biotite powder can be reproduced from the average of three  
391 spectra measured on single-crystals with appropriate orientations (see Figure 4a). However, based  
392 on our angle-dependency results, we show other ways to measure “powder-equivalent” spectra.  
393 Figure 8 summarizes the crystal positioning that is required for measuring equivalent XANES or PE

394 peaks. For example the recording of a “powder-equivalent” XANES spectrum consists of rotating  
395 the sample by 35° from *ab-ba* to *ac-bc*. Since *ab-ba* is equivalent to *ca-cb*, a rotation of 35° from  
396 *ca-cb* to *ac-bc* also leads to the same result. On the other hand, we show that a “powder-equivalent”  
397 PE edge peak is obtained when the sample is rotated by 35° from the *ac-bc* position to the *ab-ba*  
398 position. The 35° angle obtained in this study is in excellent agreement with the “magic-angle”  
399 theorem applied to X-ray absorption spectroscopy (Pettifer et al., 1990), which is defined as  $\sin^2(\theta_m)$   
400 = 1/3 (i.e.,  $\theta_m = 35.26^\circ$ ). However, the approach of the latter authors was focused on the symmetry  
401 properties of particle distributions in powdered samples, and did not consider symmetry properties  
402 related to individual crystallites. Our results show that this angle should be used only between  
403 specific crystal orientations. For example in the case of biotite and talc, a rotation of 35° from *ca-cb*  
404 to *ac-bc* results in an overestimation of the centroid energy position, and leads to a 7%  
405 overestimation of #Fe<sup>3+</sup> (based on the sine model described in Figure 7b). Similarly, a rotation of  
406 35° from *ab-ba* to *ca-cb* or *ac-bc* results in a 7% underestimate of #Fe<sup>3+</sup>. The discrepancies can be  
407 even larger if the crystals follow the *ab-ba* orientation (both electric-field vector and wavevector  
408 parallel to the (001) plane): the underestimate of #Fe<sup>3+</sup> reaches 15%. Therefore, the apparent  
409 evolution of #Fe<sup>3+</sup> with crystal orientation (for biotite or talc) is asymmetric:  $-15\% < \#Fe^{3+} < +7\%$ .  
410 It follows that the “real” #Fe<sup>3+</sup> value (equivalent powder) of phyllosilicate single-crystal of  
411 unknown orientation can be underestimated by 15%, or overestimated by 7%. For clinocllore or  
412 antigorite, the #Fe<sup>3+</sup> variability deduced from the sine model (Figure 7b) is smaller:  $-10\% < \#Fe^{3+}$   
413  $< +5\%$ . These are maximum values, and our results show that a proper orientation of the single  
414 crystals, relative to the polarized X-ray beam, leads to the reduction of the uncertainty in the  
415 determination of #Fe<sup>3+</sup> down to the intrinsic error of the method. This latter is mainly due to the  
416 error made on the determination of the centroid-energy of the pre-edge features, which is usually  
417 considered to be about 0.05 eV according to the type of baseline used (e.g., Farges, 2001; Farges et  
418 al., 2004; Wilke et al., 2001). Then, the errors propagated to the #Fe<sup>3+</sup> depend on the type of

419 coordination for the ferrous and ferric cations, as well as their respective proportions. Typically,  
420 based on the work of Wilke et al. (2001), a mixture composed of  $^{[VI]}\text{Fe}^{2+}$  and  $^{[VI]}\text{Fe}^{3+}$  will lead to  
421  $\# \text{Fe}^{3+}$  uncertainties between 0.03 (near the ferrous pole) and 0.05 (near the ferric pole).

422

423 **Acknowledgments**

424           We particularly thank Etienne Audebaud and Emmanuel Robert, in charge of the Dolomieu  
425 Mineral Collection (Grenoble, France), who generously provided the crystal samples investigated  
426 here, as well as Max Wilke (GFZ, Potsdam, Germany) for providing the model compounds for the  
427 calibration of our data. We also thank Florian Perrin (ESRF, Grenoble, France) for his precious  
428 support during data acquisition, as well as Pr. C.M.B. Henderson and the other anonymous reviewer  
429 for their helpful comments on the manuscript. Thank you to Pr. Alexandre Simionovici (ISTerre,  
430 Grenoble, France) for proofreading the manuscript. This work was entirely supported by the ESRF  
431 ID24-BM29 “In-House Research” program.

432

433

434 **References**

- 435 Andrault, D., Muñoz, M., Bolfan-Casanova, N., Guignot, N., Perrillat, J.-P., Aquilanti, G., and  
436 Pascarelli, S. (2010) Experimental evidence for perovskite and post-perovskite coexistence  
437 throughout the whole D " region. *Earth And Planetary Science Letters*, 293(1-2), 90-96.
- 438 Andréani, M., Grauby, O., Baronnet, A., and Muñoz, M. (2008) Occurrence, composition and  
439 growth of polyhedral serpentine. *European Journal of Mineralogy*, 20(2), 159-171.
- 440 Ankudinov, A., Ravel, B., Rehr, J., and Conradson, S. (1998) Real-space multiple-scattering  
441 calculation and interpretation of x-ray-absorption near-edge structure. *Physical Review B:*  
442 *Condensed Matter*, 58(12), 7565-7576.
- 443 Bajt, S., Sutton, S.R., and Delaney, J. (1994) X-ray microprobe analysis of iron oxidation-states in  
444 silicates and oxides using X-ray-absorption near-edge structure (XANES). *Geochimica et*  
445 *Cosmochimica Acta*, 58(23), 5209-5214.
- 446 Benzerara, K., Yoon, T.H., Menguy, N., Tyliczszak, T., and Brown, G.E. (2005) Nanoscale  
447 environments associated with bioweathering of a Mg-Fe-pyroxene. *Proceedings of the*  
448 *National Academy of Sciences of the United States of America*, 102(4), 979-982.
- 449 Berry, A.J., Danyushevsky, L.V., O'Neill, H.S.C., Newville, M., and Sutton, S.R. (2008) Oxidation  
450 state of iron in komatiitic melt inclusions indicates hot Archaean mantle. *Nature*, 455(7215),  
451 960-U42.
- 452 Berry, A.J., O'Neill, H.S.C., Jayasuriya, K., Campbell, S., and Foran, G. (2003) XANES  
453 calibrations for the oxidation state of iron in a silicate glass. *American Mineralogist*, 88(7),  
454 967-977.
- 455 Bolfan-Casanova, N., Munoz, M., Mccammon, C., Deloule, E., Ferot, A., Demouchy, S., France,  
456 L., Andrault, D., and Pascarelli, S. (2012) Ferric iron and water incorporation in wadsleyite  
457 under hydrous and oxidizing conditions: A XANES, Mo<sup>57</sup>ssbauer, and SIMS study.  
458 *American Mineralogist*, 97(8-9), 1483-1493.

- 459 Bordage, A., Brouder, C., Balan, E., Cabaret, D., Juhin, A., Arrio, M.A., Saintavit, P., Calas, G.,  
460 and Glatzel, P. (2010) Electronic structure and local environment of substitutional V<sup>3+</sup> in  
461 grossular garnet Ca<sub>3</sub>Al<sub>2</sub>(SiO<sub>4</sub>)<sub>3</sub>: K-edge X-ray absorption spectroscopy and first-  
462 principles modeling. *American mineralogist*, 95(8-9), 1161-1171.
- 463 Brown, G., Wang, Y., Gélabert, A., Ha, J., Cismasu, C., Ona-Nguema, G., Benzerara, K., Miot, J.,  
464 Menguy, N., and Morin, G. (2008) Synchrotron X-ray studies of heavy metal mineral-  
465 microbe interactions. *Mineralogical Magazine*, 72(1), 169-173.
- 466 Cabaret, D., Bordage, A., Juhin, A., Arfaoui, M., and Gaudry, E. (2010) First-principles  
467 calculations of X-ray absorption spectra at the K-edge of 3d transition metals: an electronic  
468 structure analysis of the pre-edge. *Physical Chemistry Chemical Physics*, 12, 5619-5633.
- 469 Canil, D., O'Neill, H.S.C., Pearson, D., Rudnick, R., McDonough, W., and Carswell, D. (1994)  
470 Ferric iron in peridotites and mantle oxidation-states. *Earth And Planetary Science Letters*,  
471 123(1-4), 205-220.
- 472 Di Benedetto, F., D'acapito, F., Fornaciai, G., Innocenti, M., Montegrossi, G., Pardi, L.A., Tesi, S.,  
473 and Romanelli, M. (2010) A Fe K-edge XAS study of amethyst. *Phys Chem Minerals*,  
474 37(5), 283-289.
- 475 Diener, J.F.A., and Powell, R. (2010) Influence of ferric iron on the stability of mineral  
476 assemblages. *Journal of Metamorphic Geology*, 28(6), 599-613.
- 477 Dräger, G., Frahm, R., Materlik, G., and Brummer, O. (1988) On the multipole character of the X-  
478 ray transitions in the pre-edge structure of Fe K-absorption spectra - An experimental-study.  
479 *Physica Status Solidi B Basic Solid State Physics*, 146(1), 287-294.
- 480 Dyar, M., Delaney, J., and Sutton, S.R. (2001) Fe XANES spectra of iron-rich micas. *European*  
481 *Journal of Mineralogy*, 13(6), 1079-1098.

- 482 Dyar, M., Gunter, M., Delaney, J., Lanzirrotti, A., and Sutton, S.R. (2002a) Use of the spindle stage  
483 for orientation of single crystals for microXAS: Isotropy and anisotropy in Fe-XANES  
484 spectra. *American Mineralogist*, 87(10), 1500-1504.
- 485 Dyar, M., Lowe, E., Guidotti, C., and Delaney, J. (2002b) Fe<sup>3+</sup> and Fe<sup>2+</sup> partitioning among  
486 silicates in metapelites: A synchrotron micro-XANES study. *American Mineralogist*, 87(4),  
487 514-522.
- 488 Farges, F. (2001) Crystal chemistry of iron in natural grandierites: an X-ray absorption fine-  
489 structure spectroscopy study. *Physics and Chemistry of Minerals*, 28(9), 619-629.
- 490 Farges, F., Brown Jr, G., Petit, P., and Muñoz, M. (2001) Transition elements in water-bearing  
491 silicate glasses/melts. Part I. A high-resolution and anharmonic analysis of Ni coordination  
492 environments in crystals, glasses, and melts. *Geochimica et Cosmochimica Acta*, 65(10),  
493 1665-1678.
- 494 Farges, F., Lefrère, Y., Rossano, S., Berthereau, A., Calas, G., and Brown Jr, G. (2004) The effect  
495 of redox state on the local structural environment of iron in silicate glasses: a combined  
496 XAFS spectroscopy, molecular dynamics, and bond valence study. *Journal of Non-  
497 Crystalline Solids*, 344(3), 176-188.
- 498 Frost, D.J., and Langenhorst, F. (2002) The oxidation state of iron in the lower mantle. *Geochimica  
499 et Cosmochimica Acta*, 66(15A), A248-A248.
- 500 Galois, L., Calas, G., and Arrio, M. (2001) High-resolution XANES spectra of iron in minerals  
501 and glasses: structural information from the pre-edge region. *Chemical Geology*, 174(1-3),  
502 307-319.
- 503 Henderson, C.M.B., Cressey, G., and Redfern, S.A.T. (1995) Geological applications of  
504 synchrotron radiation. *Radiation Physics and Chemistry*, 45(3), 459-481.

- 505 Heumann, D., Dräger, G., and Bocharov, S. (1997) Angular-dependence in the K pre-edge XANES  
506 of cubic crystals: The separation of the empty metal e(g) and t(2g) states of NiO and FeO.  
507 Journal de Physique IV, 7(C2), 481-483.
- 508 Kelley, K.A., and Cottrell, E. (2009) Water and the Oxidation State of Subduction Zone Magmas.  
509 Science, 325(5940), 605-607.
- 510 Manceau, A., Bonnin, D., Kaiser, P., and Fretigny, C. (1988) Polarized EXAFS of biotite and  
511 chlorite. Physics and Chemistry of Minerals, 16(2), 180-185.
- 512 Marcaillou, C., Muñoz, M., Vidal, O., Parra, T., and Harfouche, M. (2011) Mineralogical evidence  
513 for H<sub>2</sub> degassing during serpentinization at 300 degrees C/300 bar. Earth And Planetary  
514 Science Letters, 303(3-4), 281-290.
- 515 Marcelli, A., Cibir, G., Cinque, G., Mottana, A., and Brigatti, M. (2006) Polarized XANES  
516 spectroscopy: The K edge of layered K-rich silicates. Radiation Physics and Chemistry,  
517 75(11), 1596-1607.
- 518 McCammon, C.A., Frost, D.J., Smyth, J., Laustsen, H., Kawamoto, T., Ross, N., and Van Aken, P.  
519 (2004) Oxidation state of iron in hydrous mantle phases: implications for subduction and  
520 mantle oxygen fugacity. Physics of the Earth and Planetary Interiors, 143, 157-169.
- 521 Miot, J., Benzerara, K., Morin, G., Kappler, A., Bernard, S., Obst, M., Féraud, C., Skouri-Panet, F.,  
522 Guigner, J.-M., Posth, N., Galvez, M., Brown, G.E., and Guyot, F. (2009) Iron  
523 biomineralization by anaerobic neutrophilic iron-oxidizing bacteria. Geochimica et  
524 Cosmochimica Acta, 73(3), 696-711.
- 525 Mottana, A., Marcelli, A., Cibir, G., and Dyar, M. (2002) X-ray absorption spectroscopy of the  
526 micas. Rev Mineral Geochem, 46, 371-411.
- 527 Muñoz, M., Bureau, H., Malavergne, V., Menez, B., Wilke, M., Schmidt, C., Simionovici, A.,  
528 Somogyi, A., and Farges, F. (2005) In situ speciation of nickel in hydrous melts exposed to  
529 extreme conditions. Physica Scripta, 2005, 921.

- 530 Muñoz, M., De Andrade, V., Vidal, O., Lewin, E., Pascarelli, S., and Susini, J. (2006) Redox and  
531 speciation micromapping using dispersive X-ray absorption spectroscopy: Application to  
532 iron in chlorite mineral of a metamorphic rock thin section. *Geochemistry Geophysics*  
533 *Geosystems*, 7, Q11020.
- 534 Muñoz, M., Pascarelli, S., Aquilanti, G., Narygina, O., Kurnosov, A., and Dubrovinsky, L. (2008)  
535 Hyperspectral  $\mu$ -XANES mapping in the diamond-anvil cell: analytical procedure applied to  
536 the decomposition of (Mg,Fe)-ringwoodite at the upper/lower mantle boundary. *High*  
537 *Pressure Research*, 28(4), 665-673.
- 538 Pascarelli, S., Mathon, O., Muñoz, M., Mairs, T., and Susini, J. (2006) Energy-dispersive  
539 absorption spectroscopy for hard-X-ray micro-XAS applications. *Journal of Synchrotron*  
540 *Radiation*, 13(5), 351-358.
- 541 Petit, P., Farges, F., Wilke, M., and Solé, V. (2001) Determination of the iron oxidation state in  
542 Earth materials using XANES pre-edge information. *Journal of Synchrotron Radiation*, 8(2),  
543 952-954.
- 544 Pettifer, R., Brouder, C., Benfatto, M., Natoli, C., Hermes, C., and Lopez, M. (1990) Magic-angle  
545 theorem in powder X-ray absorption spectroscopy. *Physical Review B: Condensed Matter*,  
546 42(1), 37-42.
- 547 Pfalzer, P., Urbach, J., Klemm, M., Horn, S., denBoer, M., Frenkel, A., and Kirkland, J. (1999)  
548 Elimination of self-absorption in fluorescence hard-x-ray absorption spectra. *Physical*  
549 *Review B: Condensed Matter*, 60(13), 9335-9339.
- 550 Rehr, J., Albers, R., and Zabinsky, S. (1992) High-order multiple-scattering calculations of X-ray-  
551 absorption fine-structure. *Physical Review Letters*, 69(23), 3397-3400.
- 552 Rehr, J., Zabinsky, S., Ankudinov, A., and Albers, R. (1995) Atomic-XAFS and XANES. *Physica*  
553 *B: Condensed Matter*, 208, 23-26.

- 554 Sassi, R., Cruciani, G., Mazzoli, C., Nodari, L., and Craven, J. (2008) Multiple titanium  
555 substitutions in biotites from high-grade metapelitic xenoliths (Euganean Hills, Italy):  
556 Complete crystal chemistry and appraisal of petrologic control. *American Mineralogist*,  
557 93(2-3), 339-350.
- 558 Schmid, R., Wilke, M., Oberhänsli, R., Janssens, K., Falkenberg, G., Franz, L., and Gaab, A. (2003)  
559 Micro-XANES determination of ferric iron and its application in thermobarometry. *Lithos*,  
560 70(3-4), 381-392.
- 561 Schofield, P.F., Van Der Laan, G., Henderson, C.M.B., and Cressey, G. (1998) A single crystal,  
562 linearly polarized Fe 2p X-ray absorption study of gillespite. *Mineralogical Magazine*,  
563 62(1), 65-75.
- 564 Shulman, R., Yafet, Y., Eisenberger, P., and Blumberg, W. (1976) Observation and interpretation of  
565 X-ray absorption edges in iron compounds and proteins. *Proceedings of the National*  
566 *Academy of Sciences of the United States of America*, 73(5), 1384-1388.
- 567 Van Der Laan, G., Schofield, P.F., Cressey, G., and Henderson, C.M.B. (1996) Natural linear  
568 dichroism at the Fe 2p absorption edge of gillespite. *Chemical Physics Letters*, 252, 272-  
569 276.
- 570 Vidal, O., De Andrade, V., Lewin, E., Muñoz, M., Parra, T., and Pascarelli, S. (2006) P-T-  
571 deformation-Fe<sup>3+</sup>/Fe<sup>2+</sup> mapping at the thin section scale and comparison with XANES  
572 mapping: application to a garnet-bearing metapelite from the Sambagawa metamorphic belt  
573 (Japan). *Journal of Metamorphic Geology*, 24(7), 669-683.
- 574 Vidal, O., Parra, T., and Vieillard, P. (2005) Thermodynamic properties of the Tschermak solid  
575 solution in Fe-chlorite: Application to natural examples and possible role of oxidation.  
576 *American Mineralogist*, 90(2-3), 347-358.

- 577 Westre, T., Kennepohl, P., DeWitt, J., Hedman, B., Hodgson, K., and Solomon, E. (1997) A  
578 multiplet analysis of Fe K-edge 1s->3d pre-edge features of iron complexes. Journal of the  
579 American Chemical Society, 119(27), 6297-6314.
- 580 Wilke, M., Farges, F., Petit, P., Brown Jr, G., and Martin, F. (2001) Oxidation state and  
581 coordination of Fe in minerals: An Fe K-XANES spectroscopic study. American  
582 Mineralogist, 86(5-6), 714-730.
- 583 Wilke, M., Partzsch, G., Bernhardt, R., and Lattard, D. (2005) Determination of the iron oxidation  
584 state in basaltic glasses using XANES at the K-edge. Chemical Geology, 220(1-2), 143-161.  
585

586 **Figure captions**

587

588 **Figure 1.**  $\mu$ -XRF spectra for biotite, clinochlore, talc and antigorite showing relative abundances of  
589 the major and minor elements.

590

591 **Figure 2.** Schematic representation of the incident polarized X-ray beam relative to the orientation  
592 of the macroscopic phyllosilicate single crystal: a) *ac*-positioning, also noted  $0^\circ$  in the text; b) *ab*-  
593 positioning, also noted  $90^\circ$  in the text; c) *ca*-positioning.

594

595 **Figure 3.** Spectral signatures, at the Fe *K*-edge, for 6 different orientations of biotite single crystal  
596 relative to the linearly polarized X-ray beam. a) Theoretical (FEFF) *ab initio* calculations of the  
597 XANES spectra. b) Experimental XANES spectra and pre-edge peaks.

598

599 **Figure 4.** Experimental Fe *K*-edge XANES spectra measured for the crystals of biotite (a),  
600 clinochlore (b), talc (c) and antigorite (d), as a function of their orientation relative to the polarized  
601 incident X-ray beam. Spectra are collected from the orientation *ac-bc* to *ab-ba* by steps of  $15^\circ$ , and  
602 for the orientation *ca-cb*. For each series, the spectrum resulting from the average of *ac-bc*, *ab-ba*  
603 and *ca-cb* is shown, and compared to the spectrum obtained for the powder.

604

605 **Figure 5.** Fe *K*-edge pre-edge peaks obtained for the crystals of biotite (a), clinochlore (b), talc (c)  
606 and antigorite (d), as a function of their orientation relative to the polarized X-ray beam: from  $0^\circ$   
607 (*ac-bc*) to  $90^\circ$  (*ab-ba*) by steps of  $15^\circ$ , and for the orientation *ca-cb*. Empty circles represent the  
608 experimental data, dashed lines represent the pseudo-Voigt functions used for the fitting process,  
609 and solid lines represent the fitting results.

610

611 **Figure 6.** Integrated area vs. centroid energy variogram reporting pre-edge peak data that  
612 correspond to biotite, clinocllore, talc and antigorite measured between 0° and 90°. The diameter of  
613 the circular regions (iron-speciation end-members) is similar to that of the variogram of Wilke et al.  
614 (2001) and reflects the uncertainty of measurement.

615

616 **Figure 7.** Evolution of the pre-edge peak centroid energies (a) and the “apparent”  $\text{Fe}^{3+}/\text{Fe}_{\text{total}}$  ratios  
617 (b) as a function of the positioning angle of the samples (dots). Sine fitting functions described by  
618 Eq. 1 and 3 are represented with lines. Values obtained for powdered samples intersect the sine  
619 functions at a “powder-equivalent” angle of 35°.

620

621 **Figure 8.** Sketch showing appropriate positioning of phyllosilicate single crystals that allow  
622 measuring “equivalent-powder” XANES spectra (upper part) and pre-edge peaks (lower part). The  
623 sketch view is from the incident X-ray beam. The arrows indicate rotations to apply in order to  
624 obtain powder-like spectra.

625

626

627

628 **Table 1.**  $\mu$ -XRF chemical analyses (wt.% and a.f.p.u.) for the biotite, clinochlore, talc and  
 629 antigorite single crystals.

630

(wt.%)	biotite	clinochlore	talc	antigorite
SiO <sub>2</sub>	39.57 ± 0.66	33.92 ± 1.02	62.15 ± 1.86	41.53 ± 1.25
TiO <sub>2</sub>	1.59 ± 0.02	0.03 ± 0.00	0.00 ± 0.00	0.05 ± 0.00
Al <sub>2</sub> O <sub>3</sub>	14.51 ± 0.14	8.18 ± 0.24	0.63 ± 0.02	1.12 ± 0.03
Cr <sub>2</sub> O <sub>3</sub>	0.00 ± 0.00	0.66 ± 0.02	0.00 ± 0.00	0.13 ± 0.00
Fe <sub>2</sub> O <sub>3</sub>	-	-	-	1.16 ± 0.03
FeO	3.88 ± 0.12	2.86 ± 0.09	1.28 ± 0.04	-
MnO	0.03 ± 0.00	0.02 ± 0.00	0.00 ± 0.00	0.07 ± 0.00
NiO	0.00 ± 0.00	0.13 ± 0.00	0.05 ± 0.00	0.05 ± 0.00
MgO	25.63 ± 0.77	40.86 ± 1.23	30.73 ± 0.92	42.91 ± 1.29
CaO	0.05 ± 0.00	0.01 ± 0.00	0.00 ± 0.00	0.00 ± 0.00
K <sub>2</sub> O	10.62 ± 0.32	0.02 ± 0.00	0.00 ± 0.00	0.00 ± 0.00
H <sub>2</sub> O	4.20 ± 0.13	12.55 ± 0.38	4.70 ± 0.14	12.81 ± 0.38
Total	100.08	99.24	99.54	99.83
(a.p.f.u.)	biotite	clinochlore	talc	antigorite
Si	2.80 ± 0.08	3.24 ± 0.10	3.97 ± 0.12	1.92 ± 0.06
Ti	0.08 ± 0.00	0.00 ± 0.00	0.00 ± 0.00	0.00 ± 0.00
Al	1.21 ± 0.04	0.92 ± 0.03	0.05 ± 0.00	0.06 ± 0.00
Cr	0.00 ± 0.00	0.05 ± 0.00	0.00 ± 0.00	0.00 ± 0.00
Fe(III)	-	-	-	0.04 ± 0.00
Fe(II)	0.23 ± 0.01	0.23 ± 0.01	0.07 ± 0.00	-
Mn	0.00 ± 0.00	0.00 ± 0.00	0.00 ± 0.00	0.00 ± 0.00
Ni	0.00 ± 0.00	0.01 ± 0.00	0.00 ± 0.00	0.00 ± 0.00
Mg	2.70 ± 0.08	5.82 ± 0.17	2.92 ± 0.09	2.96 ± 0.09
Ca	0.00 ± 0.00	0.00 ± 0.00	0.00 ± 0.00	0.00 ± 0.00
K	0.96 ± 0.03	0.00 ± 0.00	0.00 ± 0.00	0.00 ± 0.00
H <sub>2</sub> O	0.98 ± 0.06	3.99 ± 0.24	1.00 ± 0.06	1.96 ± 0.12
O	11	14	11	7

631

632

633

634 **Table 2.** Centroid energy ( $\pm 0.05$  eV) and integrated area ( $\pm 0.025$ ) of the pre-edge peaks, as well as  
 635 the apparent  $\#Fe^{3+}$  ( $\pm 0.03$ ) obtained for six orientations of the biotite crystal.

636

biotite crystal orientation	centroid position (eV)	integrated area	$\#Fe^{3+}$
<i>ca</i>	7113.68	0.083	0.242
<i>cb</i>	7113.68	0.085	0.242
<i>ab</i>	7113.23	0.079	0.000
<i>ba</i>	7113.26	0.086	0.010
<i>ac</i>	7113.67	0.096	0.235
<i>bc</i>	7113.69	0.106	0.245

637

638

639

640

641 **Table 3.** Centroid energy ( $\pm 0.05$  eV), integrated area ( $\pm 0.025$ ) and corresponding  $\#Fe^{3+}$  values  
 642 (from  $\pm 0.03$  to  $\pm 0.05$  for ferrous and ferric iron, respectively), obtained from pre-edge peaks of  
 643 biotite, clinocllore, talc and antigorite depending on the type of measurement (see explanations in  
 644 text).

645

	centroid energy (eV)				integrated area				#Fe <sup>3+</sup>			
	Bt	Cli	Tc	Ant	Bt	Cli	Tc	Ant	Bt	Cli	Tc	Ant
0°	7113.68	7113.66	7113.62	7114.52	0.096	0.093	0.080	0.113	0.242	0.231	0.207	0.872
15°	7113.63	7113.64	7113.74	7114.50	0.096	0.091	0.105	0.128	0.209	0.215	0.278	0.858
30°	7113.51	7113.57	7113.66	7114.45	0.082	0.086	0.083	0.119	0.140	0.178	0.229	0.808
45°	7113.46	7113.48	7113.53	7114.41	0.087	0.083	0.077	0.128	0.111	0.121	0.150	0.775
60°	7113.35	7113.45	7113.39	7114.38	0.081	0.087	0.080	0.110	0.053	0.111	0.074	0.750
75°	7113.28	7113.42	7113.36	7114.36	0.077	0.089	0.090	0.136	0.020	0.091	0.057	0.735
90°	7113.27	7113.42	7113.30	7114.34	0.084	0.093	0.075	0.117	0.014	0.091	0.027	0.713
ca-cb	7113.67	7113.70	7113.63	7114.49	0.094	0.094	0.089	0.123	0.243	0.262	0.221	0.861
average	7113.54	7113.59	7113.51	7114.45	0.091	0.093	0.081	0.118	0.165	0.195	0.152	0.821
powder	7113.52	7113.56	7113.48	7114.43	0.089	0.094	0.096	0.128	0.155	0.173	0.139	0.808

646

647

648

649

650

651

652 **Table 4.** Parameters  $\alpha$ ,  $\beta$ ,  $\gamma$  and  $\delta$ , fitted from Equations 1 and 3 for biotite, clinochlore, talc and  
 653 antigorite.  $E_{\text{eq}}$  and  $\#\text{Fe}^{3+}_{\text{eq}}$  are “powder-equivalent” values (i.e., at the  $35^\circ$  angle) for the centroid  
 654 energy and the  $\text{Fe}^{3+}/\text{Fe}_{\text{total}}$  ratio, respectively.

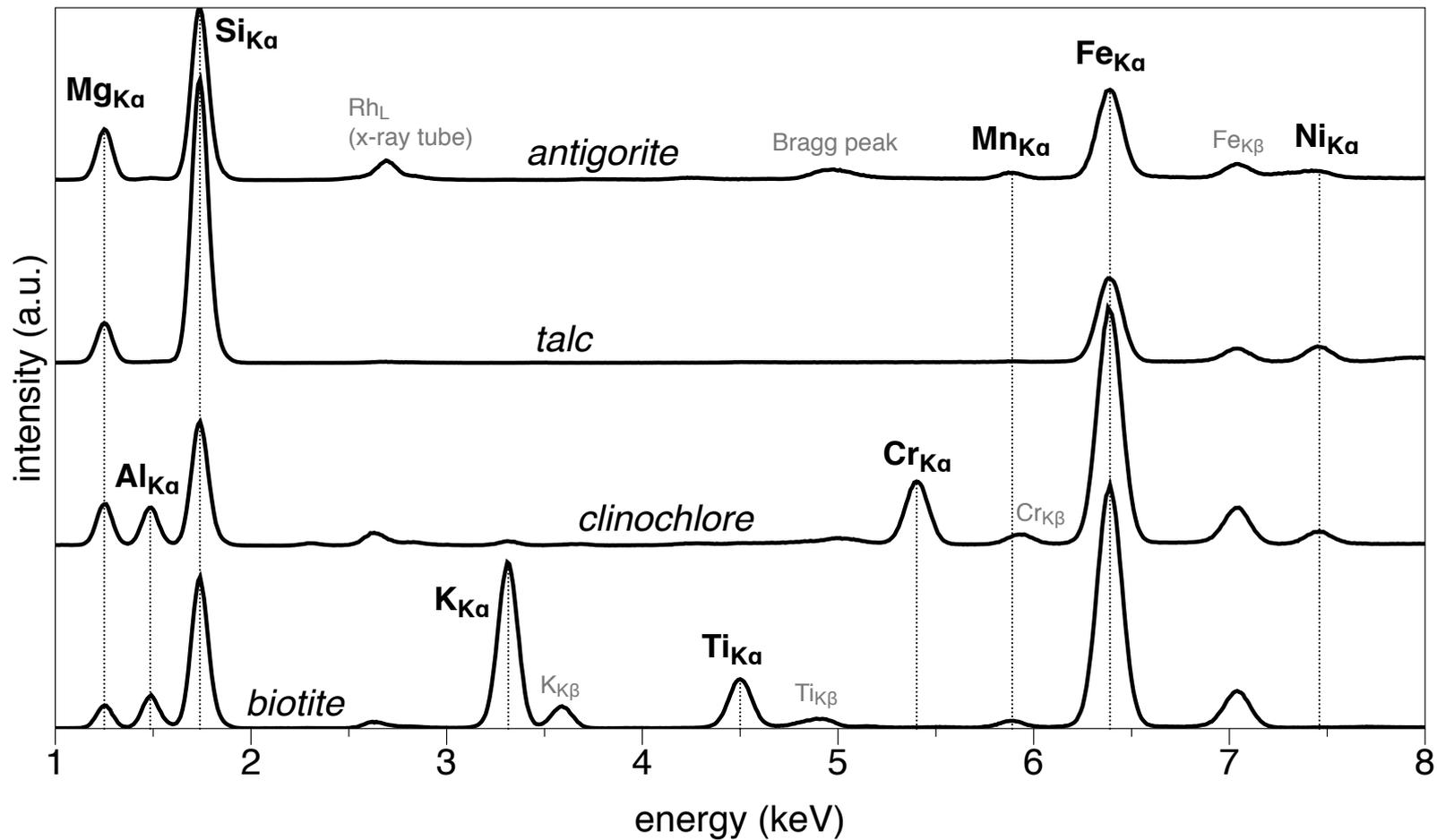
655

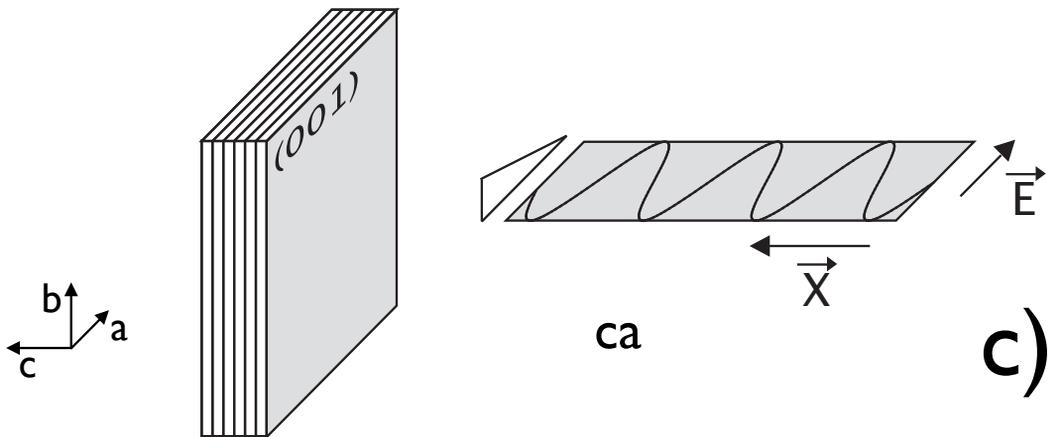
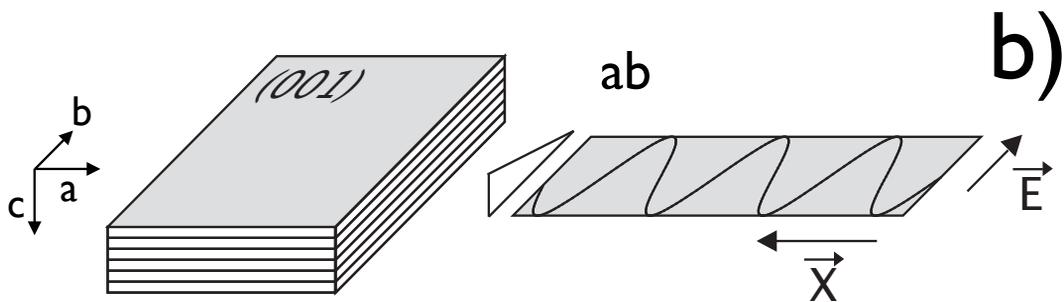
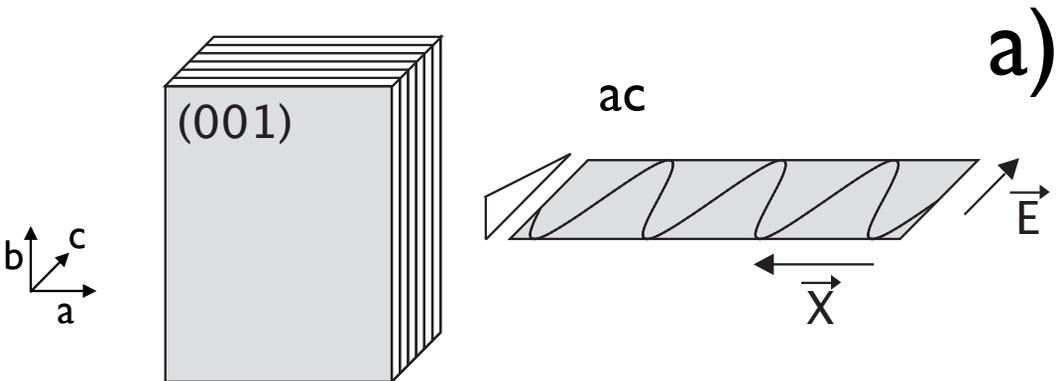
	biotite	clinochlore	talc	antigorite
$\alpha$ (eV)	$7113.45 \pm 0.05$	$7113.52 \pm 0.05$	$7113.51 \pm 0.05$	$7114.42 \pm 0.05$
$\beta$ (eV)	$0.197 \pm 0.01$	$0.122 \pm 0.01$	$0.198 \pm 0.01$	$0.082 \pm 0.01$
$2\beta$ (eV)	$0.39 \pm 0.02$	$0.25 \pm 0.02$	$0.40 \pm 0.02$	$0.16 \pm 0.02$
$E_{\text{eq}}$ (eV)	$7113.52 \pm 0.05$	$7113.56 \pm 0.05$	$7113.58 \pm 0.05$	$7114.45 \pm 0.05$
$\gamma$	$0.113 \pm 0.03$	$0.147 \pm 0.03$	$0.146 \pm 0.03$	$0.787 \pm 0.05$
$\delta$	$0.108 \pm 0.01$	$0.070 \pm 0.01$	$0.111 \pm 0.01$	$0.073 \pm 0.01$
$2\delta$	$0.22 \pm 0.02$	$0.14 \pm 0.02$	$0.22 \pm 0.02$	$0.15 \pm 0.02$
$\#\text{Fe}^{3+}_{\text{eq}}$	$0.15 \pm 0.03$	$0.17 \pm 0.03$	$0.18 \pm 0.03$	$0.81 \pm 0.05$

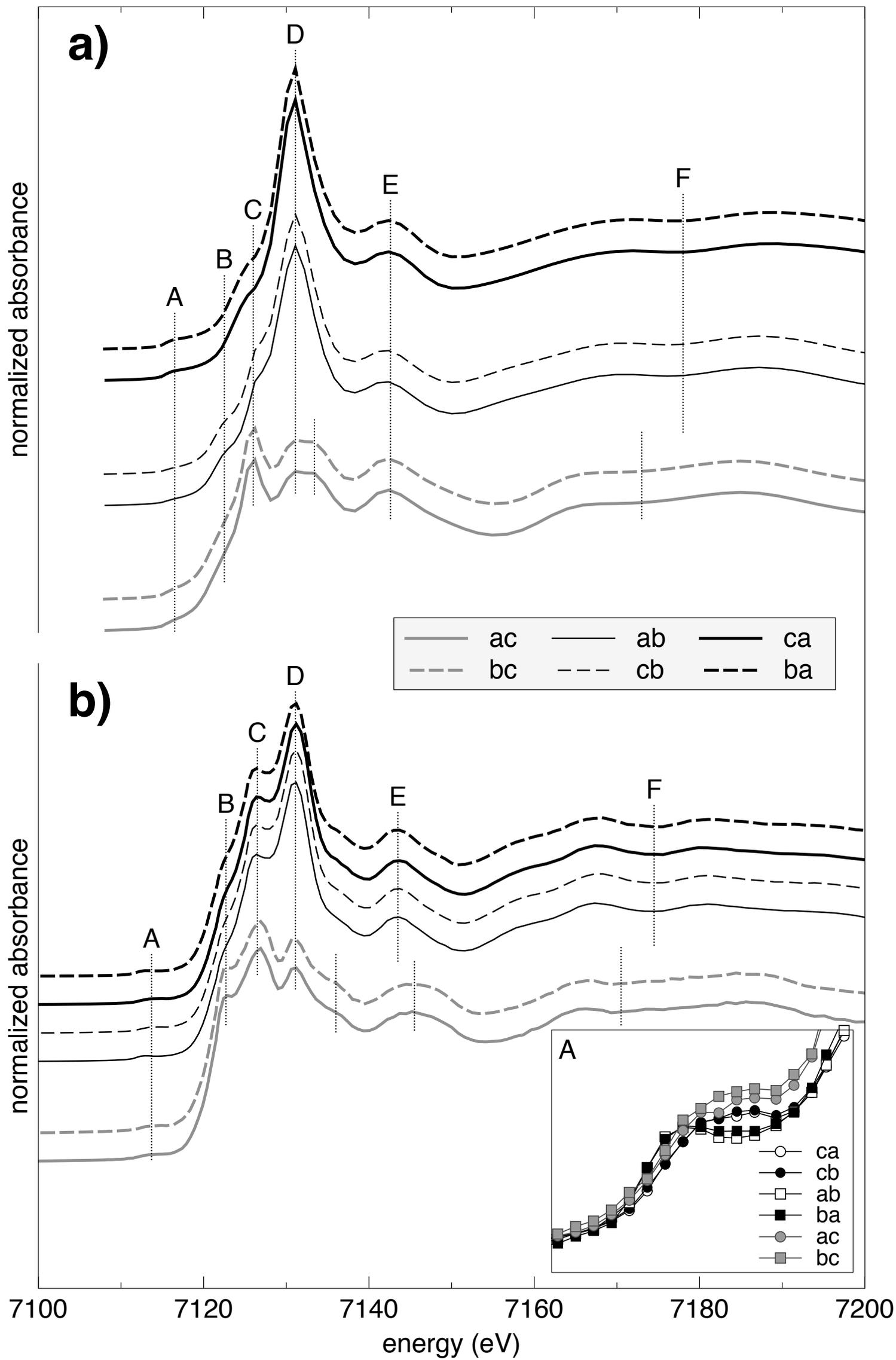
656

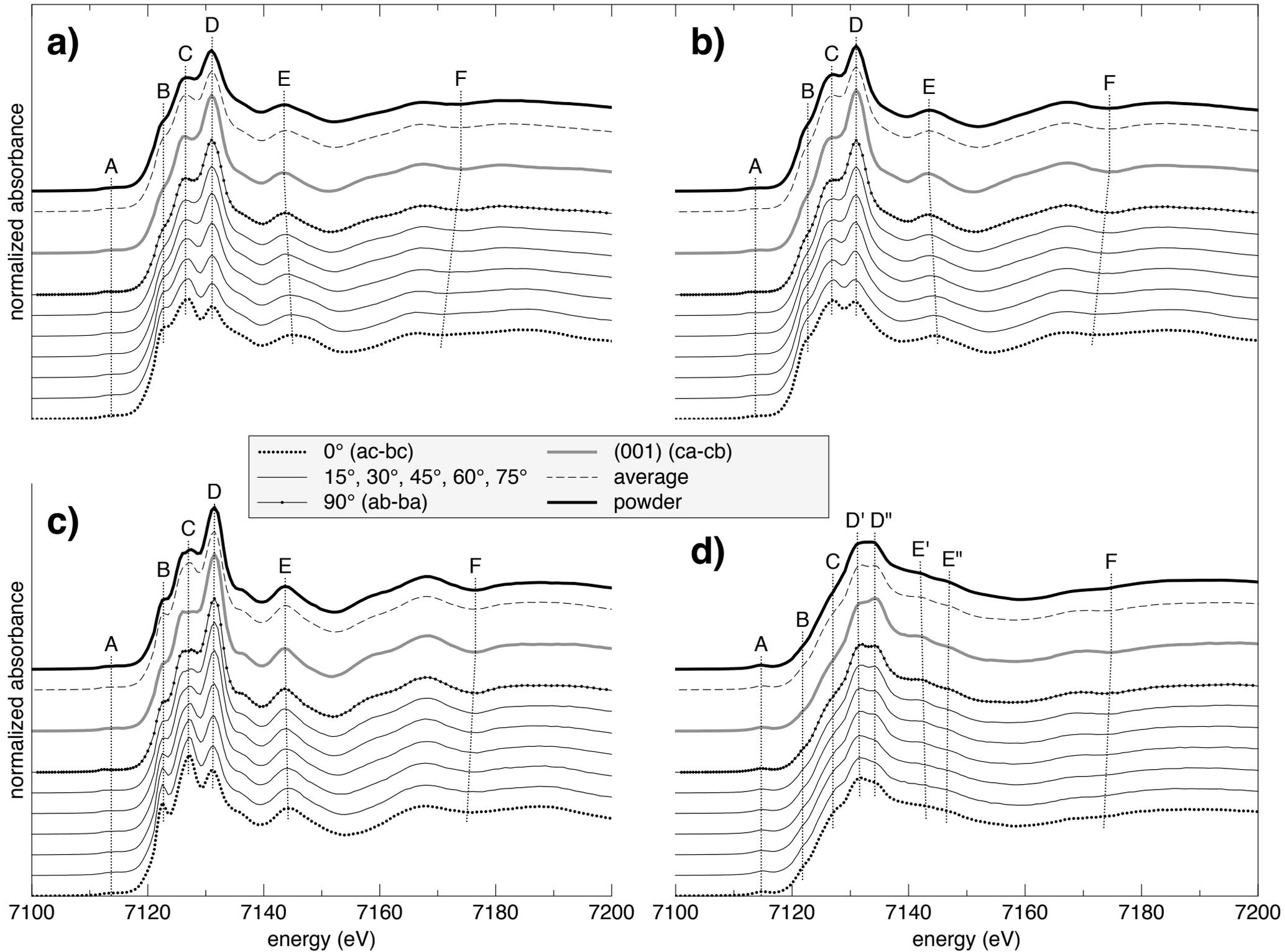
657

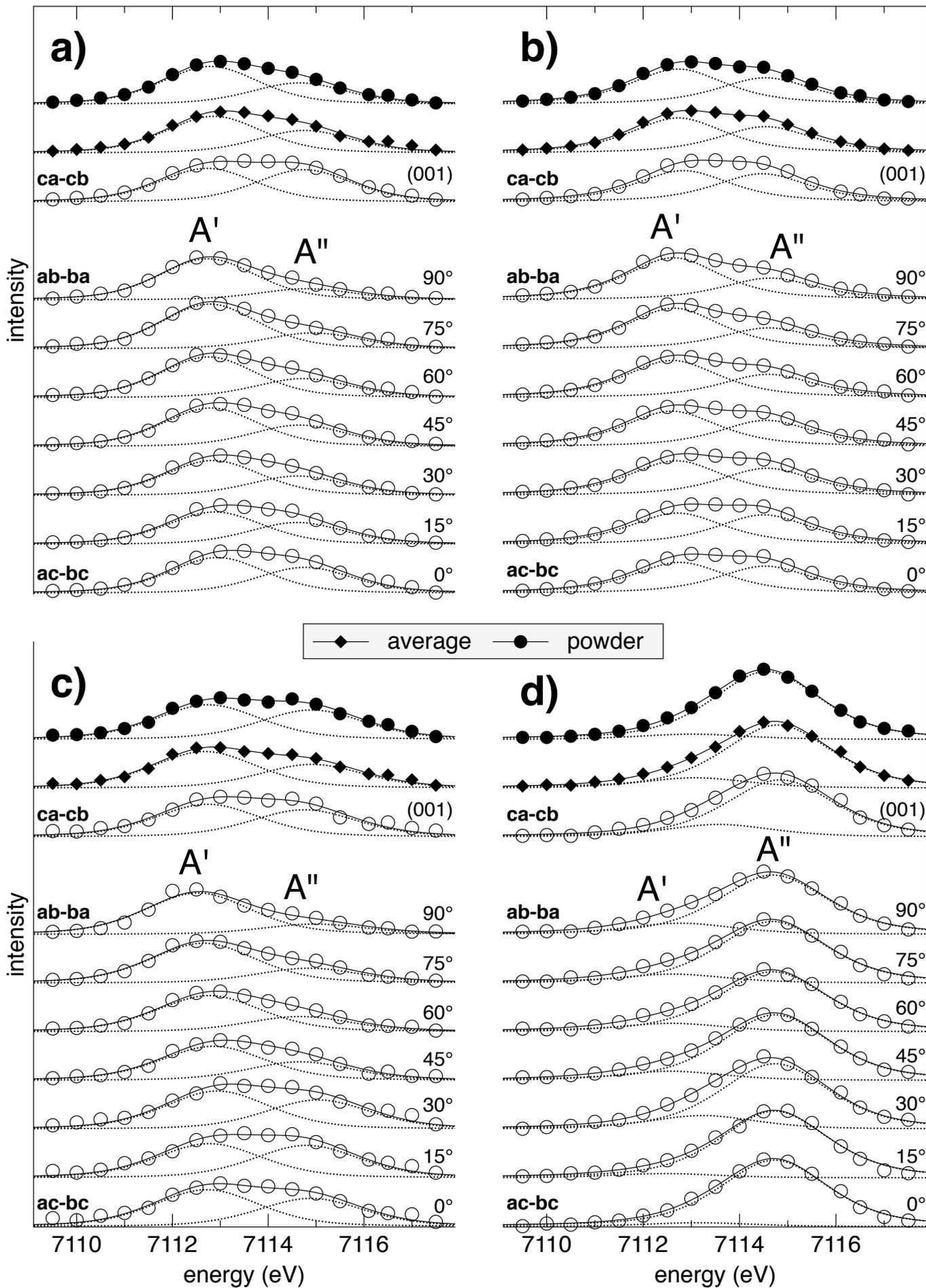
658

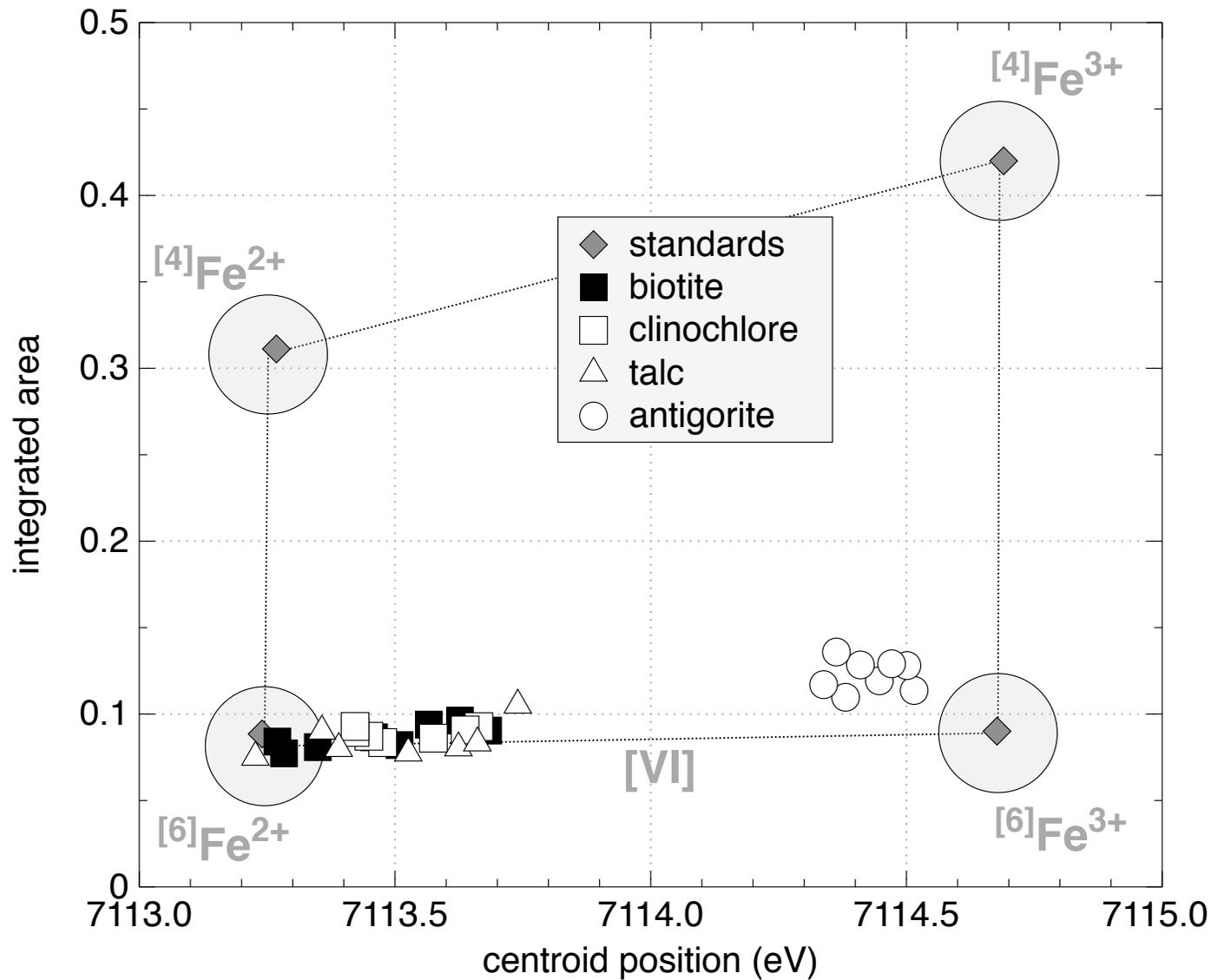


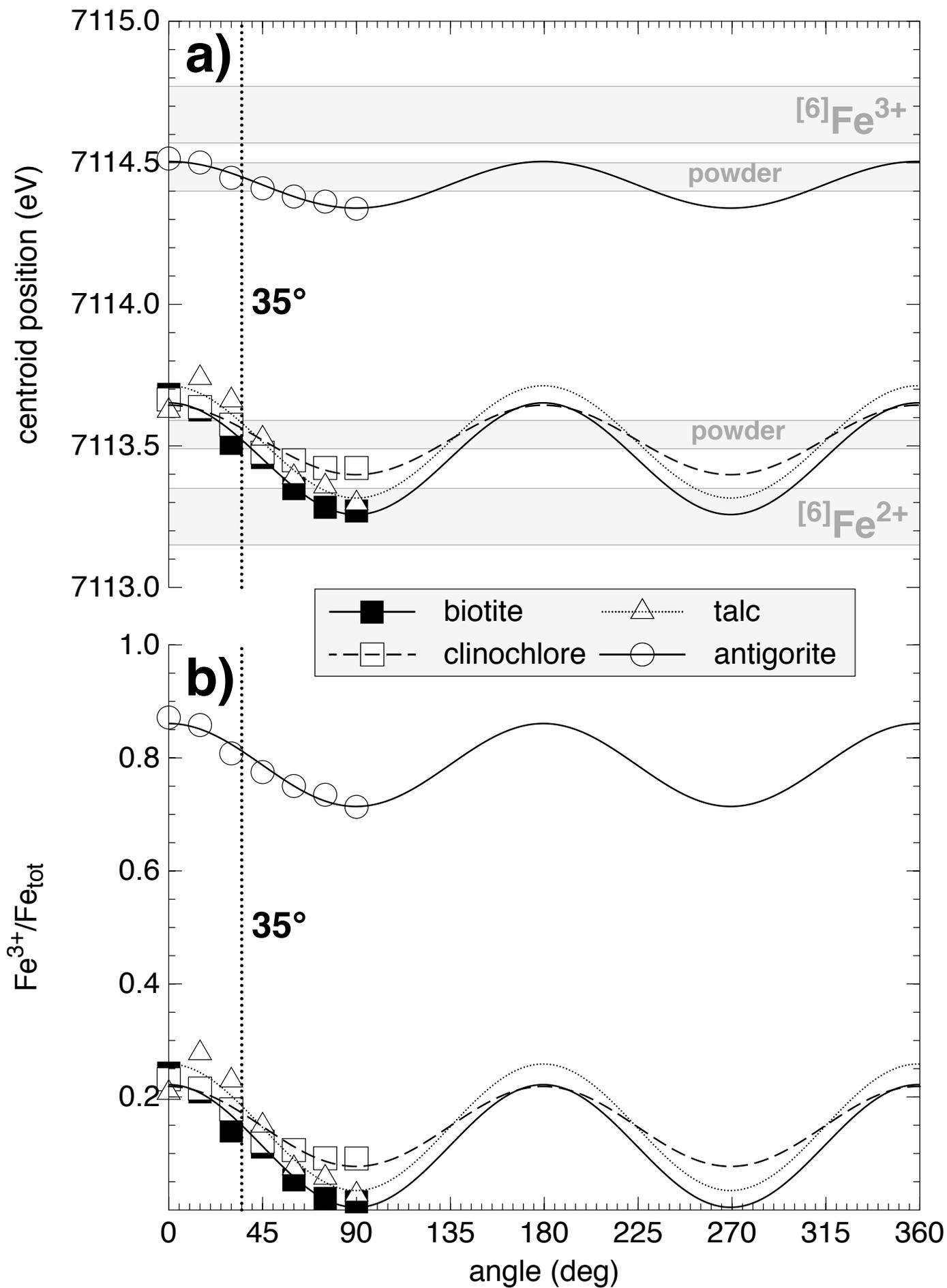




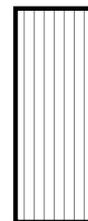
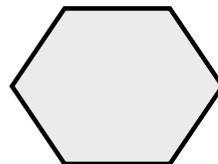
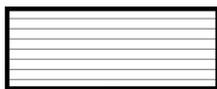




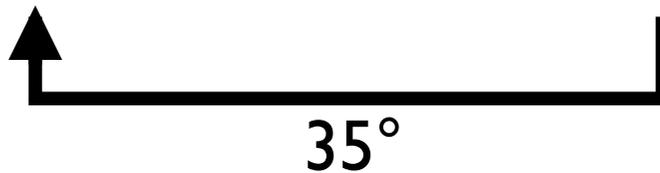




XANES



Pre-peaks



35°

35°

